ELSEVIER

Intermetallics 10 (2002) 555–570

Intermetallics

www.elsevier.com/locate/intermet

Oxidation behavior of extruded $Mo_5Si_3B_x$–$MoSi_2$–MoB intermetallics from 600°–1600 °C

Andrew J. Thom*, Eric Summers[1], Mufit Akinc

Ames Laboratory and Department of Materials Science & Engineering, Iowa State University, Ames, IA 50011, USA

Accepted 19 February 2002

Abstract

The oxidation behavior of $Mo_5Si_3B_x$ (T1)–$MoSi_2$–MoB composites fabricated by green extrusion processing was investigated over the temperature range of 600–1600 °C in air. Low temperature experiments from 600 to 1000 °C revealed that unoxidized material initially forms a mixed molybdenum and silicon oxide scale. The unoxidized material undergoes rapid mass loss over a narrow temperature range of 660–760 °C, with complete disintegration of the material occurring at about 730 °C. At temperatures above about 760 °C, a coherent glassy scale forms to protect the alloy from further oxidation. High temperature oxidation tests from 1150 to 1600 °C show that the material forms a continuous glassy scale, 10–20 μm in thickness, which protects the underlying alloy. Steady state oxidation kinetics were not achieved until exposure at 1600 °C, due to the effect of contamination introduced during green extrusion processing. The calculated parabolic rate constant at 1600 °C is 9.7×10^{-3} $mg^2/cm^4/h$, which compares favorably to that of $MoSi_2$-based materials. The observed oxidation behavior and kinetics over the entire temperature range were not significantly influenced by sample porosity (79% versus 96% of theoretical density). Boron depletion of the near-surface scale was observed at 1150 °C, leading to the formation of pure silica in the outer portion of the scale. The extent and rate of boron evaporation increased significantly as temperature increased to 1600 °C. Formation of pure silica in the scale implies that oxygen transport through silica must be the rate-limiting step in the high temperature oxidation of these alloys. © 2002 Elsevier Science Ltd. All rights reserved.

Keywords: A. Intermetallics; A. Molybdenum silicide; B. Oxidation; C. Extrusion

1. Introduction

Processing and development of high temperature ceramic and intermetallic materials places an increased burden on current-generation furnaces based on $MoSi_2$ heating elements, which permit continuous furnace operation to about 1700 °C. While newly refined $MoSi_2$-based element compositions have pushed furnace temperatures to about 1800 °C, further increases are unlikely. Element temperature is practically limited to about 1900 °C based on the $\alpha\rightarrow\beta$ transformation and possible liquid formation for off-stoichiometry compositions [1]. For operating beyond these temperatures, tungsten and graphite heating element furnace designs are used. Furnaces based on tungsten and graphite heating elements reliably operate well in excess of 1700 °C, but they suffer from significant design constraints and require a non-oxidizing environment. Their cost is also considerably more than that of current-generation molybdenum disilicide furnaces. Zirconia-based heating element furnaces have been designed for operation in air at temperatures exceeding 2000 °C. However, these furnaces are very expensive, and zirconia heating element performance above 2000 °C is unreliable. With very limited demand, zirconia heating element furnaces are only available as a custom ordered item [2].

In-situ multiphase composites of $Mo_5Si_3B_x$ (T1)–$MoSi_2$–MoB and T1–Mo_3Si–Mo_5SiB_2 (T2) offer an interesting alternative to $MoSi_2$-based alloys. These composites have an attractive combination of higher creep strength [3] with oxidation resistance comparable to $MoSi_2$ [4,5]. These multiphase composites also show improved strength compared to $MoSi_2$ [6]. Flexural strength values as high as 700 MPa were observed at elevated temperatures, and creep tests confirmed the preliminary work that showed these alloys are highly creep resistant. The room temperature fracture toughness for these composites remains low, ranging from 2

* Corresponding author.
E-mail address: ajthom@ameslab.gov (A.J. Thom).
[1] Present address: Wellman Dynamics, Creston, IA 50801, USA.

0966-9795/02/$ - see front matter © 2002 Elsevier Science Ltd. All rights reserved.
PII: S0966-9795(02)00034-1

to 4 MPa $m^{1/2}$, and so a considerable amount of work is underway to study the enhancement of fracture toughness of these composites by the incorporation of molybdenum metal. Perepezko's group has investigated the two-phase field of molybdenum metal coexisting with the T2 phase [7,8]. Schneibel et al. at Oak Ridge National Laboratory (ORNL) has evaluated the mechanical properties of the phase assemblage Mo–Mo_3Si–T2 [9,10], and also a more silicon-rich composition within the phase assemblage T1–T2–Mo_3Si for processing and strength [11]. Pratt & Whitney has been working for several years to develop molybdenum metal bearing alloys [12]. The metal phase containing assemblages, in particular Mo–T2–Mo_3Si and Mo–T2, have higher fracture toughness values of about 15 MPa $m^{1/2}$ at room temperature. However, they also suffer from decreased oxidative stability. The current thought for using these materials in high temperature structural applications is to coat a refractory substrate of the Mo-rich alloy with a T1-based alloy [12]. The refractory substrate would provide enhanced elevated temperature strength and fracture toughness while the T1-based coating would protect the substrate material from the aggressive combustion environment. In this regard, understanding the low and high temperature oxidation of T1-based materials is crucial since development of the T1-based material as a thermal barrier coating for the Mo-rich compositions is foreseen.

Ames Laboratory has also worked to develop advanced heating elements based on the T1 phase. In a heating element demonstration of extruded Mo–Si–B material [13], the element was heated at about 60 °C/min to 1300 °C and held at temperature for 10 min and allowed to naturally cool to ambient temperature. The element demonstrated thermal shock resistance as it did not crack after 12 similar cycles. The power loading for the element was as high as 194 W/cm^2, far in excess of that recommended for conventional $MoSi_2$ elements.

The objective of the present work is to study the low and high temperature oxidative stability of a Mo–Si–B composite fabricated by the low temperature green extrusion process. Extrusion is the technique that is used to fabricate $MoSi_2$-based heating elements, and so these new compositions must be amenable to the green extrusion process without suffering reduced oxidation resistance. The effect of sample density on oxidation resistance is also investigated since commercial $MoSi_2$ heating elements are processed to less than 80% of theoretical density, and the susceptibility of $MoSi_2$ to "pest" oxidation is known to depend on density.

2. Experimental procedure

Samples with a composition of approximately 70 vol% T1, 20 vol% $MoSi_2$, and 10 vol% MoB were produced by a green extrusion and sintering process presented elsewhere [13,14]. Material having both low and high relative density was prepared by sintering at different temperatures. After sintering, the diameter of the extruded material was about 3.3 mm, and approximately 1 cm long test specimens were cut from sintered rods. The phase assemblage of the sintered material was quantified by analysis of the powder X-ray diffraction (XRD) pattern using a Rietveld refinement program (GSAS, Los Alamos National Laboratory, 1985).

To quantitatively measure the mass change of unoxidized material on initial heat up from room temperature, sintered material was analyzed using a commercial horizontal beam, simultaneous thermogravimetric analyzer/differential thermal analyzer (TGA/DTA). Small samples of less than 100 mg were contained in alumina pans and heated to 1000 °C in flowing breathing air with an alumina powder reference.

For low temperature oxidation tests, the rods were placed vertically in an alumina boat inside a quartz tube

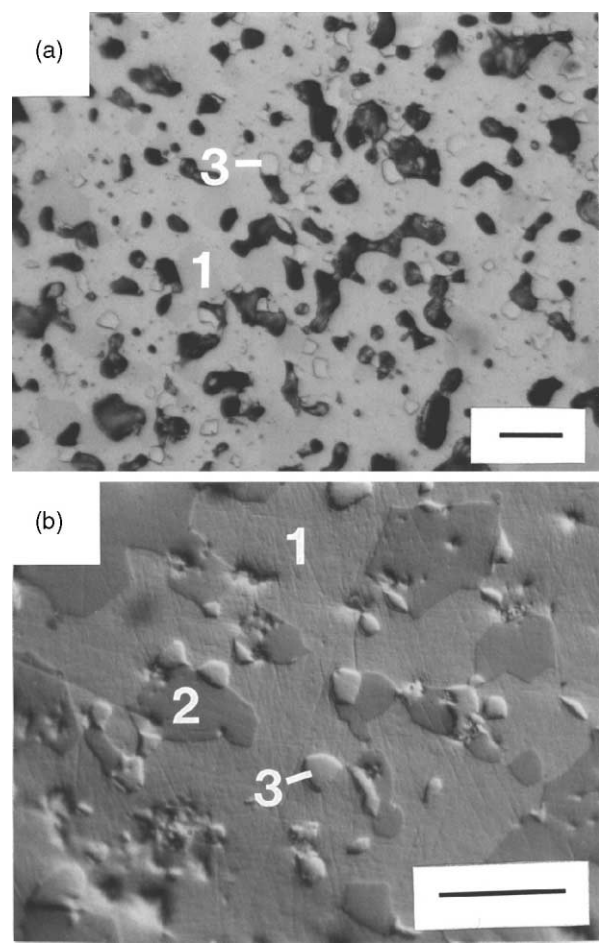

Fig. 1. Optical micrograph for as-sintered material showing (a) brightfield view of material having low relative density (79%), and (b) Nomarski contrast view of material having high relative density (96%). Key: 1 = $Mo_5Si_3B_x$ (T1) matrix, 2 = $MoSi_2$, and 3 = MoB. Bar length is 20 μm.

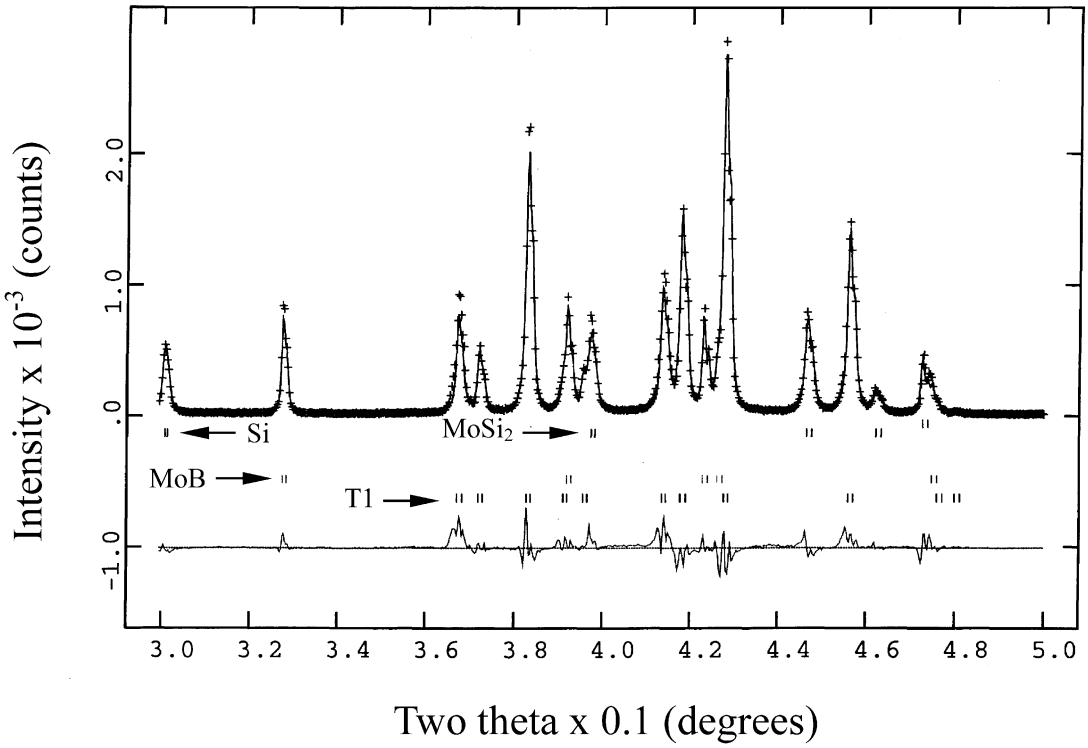

Fig. 2. Results for XRD/GSAS analysis performed on a sintered high-density sample. The observed data is shown by + marks with the calculated pattern plotted as an overlapping solid line. The ‖ markers designate reflection positions for the three phases (T1, $MoSi_2$, and MoB) and for the silicon internal standard SRM640b. The bottom plot shows the difference plot between the observed and calculated patterns. Typical ${}_wR_p$ values ranged from 0.17 to 0.21.

within a horizontal tube furnace. Samples were heated and cooled in the ambient atmosphere at 10 °C/min. Material was tested from 617 to 1001 °C, with samples cooled to room temperature for mass measurement after 5, 15, 35, 75, and 155 h of cumulative exposure. Prior to testing, samples were ultrasonically cleaned in acetone, followed by methanol, and then dried in an oven at 110 °C for 12–24 h.

For the high temperature oxidation tests, a 0.2 mm diameter hole was drilled through each sample by electro-discharge machining (EDM). Samples were cleaned as described above. Samples were then suspended from a sapphire wire in a vertical tube TGA employing an electrobalance sensitive to 1×10^{-6} g. Material was tested from 1150 to 1600 °C, with samples heated to the test temperature at 20 °C/min under flowing compressed air at a rate of 100 ml/min. Changes in the mass were recorded continuously for up to 250 h at the respective temperature.

Scanning electron microscopy combined with energy dispersive spectroscopy (SEM/EDS) was used to study the scale microstructure. The detection of boron by EDS is difficult, and so only the silicon and oxygen components of the boron modified silica scale were measured. Electron spectroscopy for chemical analysis (ESCA) and high resolution Auger electron spectroscopy (AES) were used to qualitatively determine the composition of the oxide scale, including its boron content. For ESCA measurements, the depth of the measurement into the scale was calculated from the total etch time, using an estimate of 4.5 nm per minute as determined from an etch rate monitor wafer of silica on silicon. For AES measurements, elemental concentrations through the oxide scale cross-section were estimated from line scan profiles. Samples were fractured in-situ prior to the line scan to minimize the effect of surface contamination such as adventitious carbon.

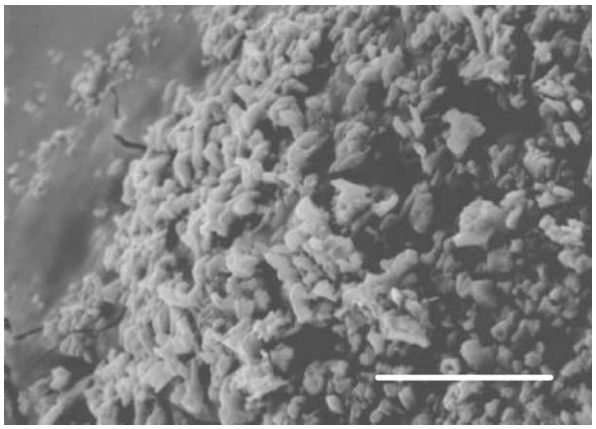

Fig. 3. SEM image (secondary electron) of the surface of the low-density sample, oxidized at 1150 °C for 155 h, showing an area of titanium-rich surface contamination. Bar length is 100 μm.

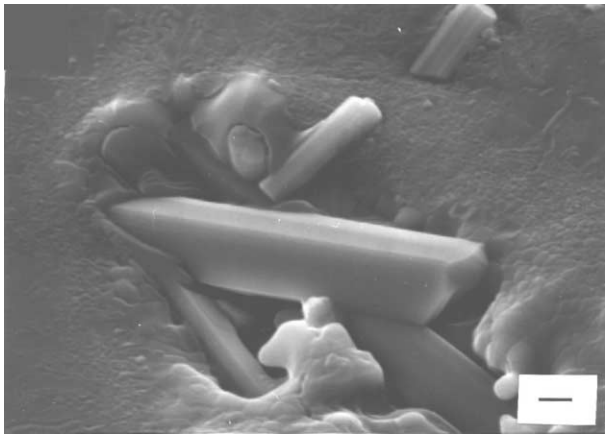

Fig. 4. SEM image (secondary electron) of the surface of the low-density sample, oxidized at 1150 °C for 155 h, showing growth of columnar grains from the surface. Incomplete formation of the scale around these grains is the likely cause of slow mass loss at 1150 °C. Bar length is 1 μm.

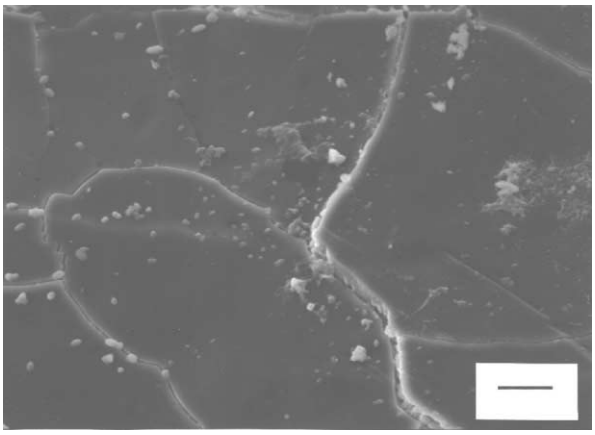

Fig. 5. SEM image (secondary electron) of the surface of the low-density sample oxidized at 1600 °C. Bar length is 10 μm.

3. Results

3.1. Microstructure and processing related contamination

Fig. 1a and b show an optical micrograph of the as-consolidated, low- and high-density material. For both materials, MoB and $MoSi_2$ are dispersed within the T1 matrix. The extent of interconnected porosity in the low-density material of Fig. 1a is evident, in contrast to the isolated porosity and occasional grain pullout seen in the high-density material of Fig. 1b. For these materials, Archimedes-type liquid immersion measurements reveal that the low-density material was about 79% of theoretical density while the high-density material was about 96% of theoretical density, where $\rho_{th} \sim 7.86$ g/cm^3. Theoretical density was calculated from the phase assemblage as quantitatively determined by XRD/GSAS analysis of the sintered materials. Fig. 2 shows a portion of the XRD scan from 30 to 50° 2Θ and the corresponding results of the GSAS refinement for the high-density material. The measured phase assemblage for both materials was very similar, ranging from 68 to 70 vol% T1, 20 to 21 vol% $MoSi_2$, and 10 to 11 vol% MoB.

Contamination was introduced into the material during the green extrusion process. The extruder screws used contain a TiN abrasion resistant coating. There was visible deterioration of the surface of the screws after extrusion, suggesting contamination of the extruded material by the TiN coating and the alloy components of the stainless steel screws. Fig. 3 shows an example of the contamination found on the scale of the high-density sample oxidized at 804 °C. The contamination appears as areas of fine, micron-sized particles that are both isolated and grouped into clusters. EDS analysis shows this debris contains significant titanium and lesser amounts of iron, molybdenum, magnesium, and calcium. Fig. 4 shows an example of the contamination found on the scale of the low-density sample oxidized at 1150 °C. Frequent areas of columnar grains are found both buried within and protruding from the scale. EDS analysis reveals the grains to contain predominantly titanium and oxygen, presumably as rutile. The titanium-containing debris seen in Fig. 3 likely contributed to the formation of these columnar grains at 1150 °C. Fig. 5 shows the surface of the low-density sample oxidized at 1600 °C. The scale is extensively cracked and contains particulate debris. EDS analysis of the debris reveals that particles near or in the crack region are rich in calcium. EDS analysis also detected calcium within the bulk Mo–Si–B alloy underlying the scale. This suggests that calcium is a contaminate that was introduced during the extrusion process. ESCA analysis of the scale formed on the high-density sample oxidized at 1600 °C revealed the presence of about 0.9 at.% aluminum. The aluminum was not detected at the interior of the underlying Mo–Si–B alloy. The aluminum was likely introduced by incomplete removal of alumina powder from the surface of the material during the process of debinding the green-extruded material [13].

As later discussed in Section 3.3, these contaminants do not impede the formation of a protective borosilicate glassy scale. However, their presence does affect the interpretation of the measured rate constants at temperatures $T \geqslant 1150$ °C.

3.2. Low temperature oxidation behavior

Upon initial heating from room temperature, all samples undergo a transient mass gain and subsequent mass loss. Fig. 6 shows a typical TGA curve for this

transient behavior for both low-density and high-density material. The TG curve is plotted as a percentage change from the initial mass of the sample. The increased surface area of the low-density sample is apparent from its seven-fold increase in percentage mass gain compared to the high-density sample. The maximum mass gain occurs between about 730 and 745 °C, and above this temperature both samples begin to show a mass loss. Fig. 7 shows the simultaneous DTA signal for the TG curves of the two samples in Fig. 6. The DTA baseline signal for an empty sample and reference pan heated under identical conditions has

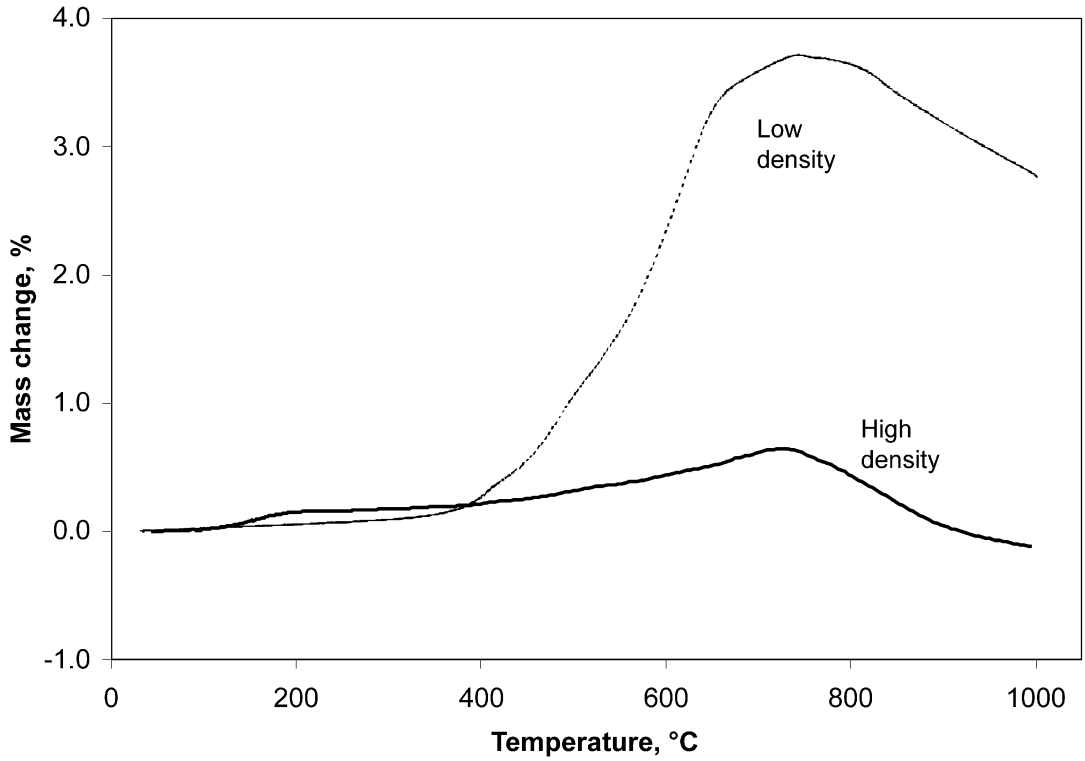

Fig. 6. Mass change on initial heating of unoxidized low- and high-density material in flowing compressed air.

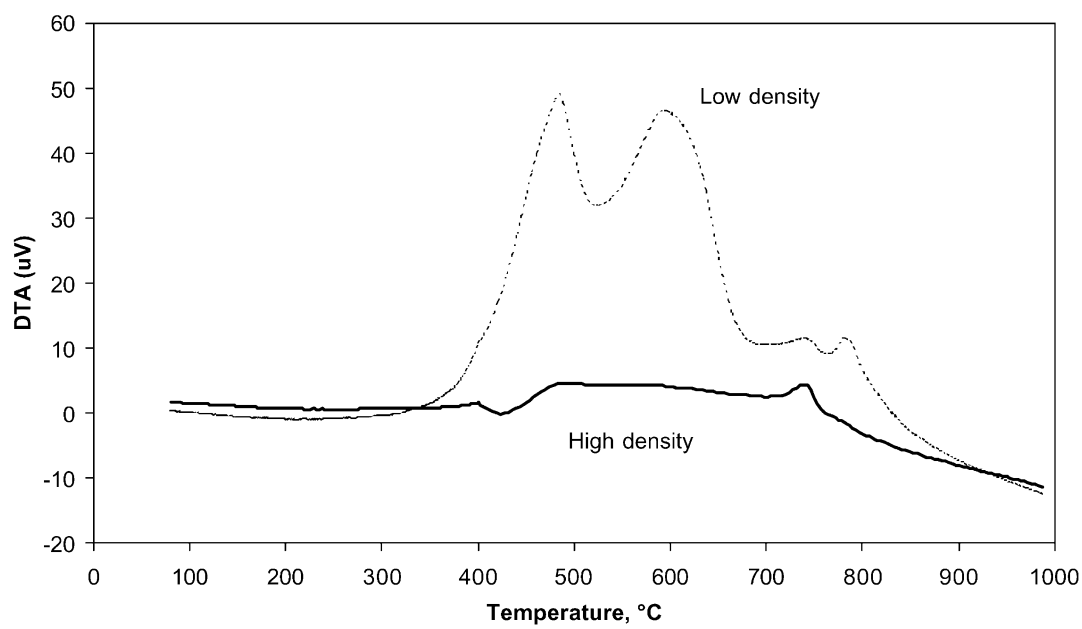

Fig. 7. DTA plot of samples from Fig. 6 on initial heating of unoxidized material. Exothermic peaks are positive.

been subtracted from each plot. The high-density sample shows a discontinuity at about 400 °C, which corresponds to an increase in the heating rate from 10 to 20 °C/min. The high-density sample shows only a slight exothermic peak at about 730 °C in an otherwise eventless plot. The magnitude of oxidation in the high-density sample is below the detection threshold of the DTA. In contrast, the low-density sample shows two large and broad exothermic peaks at about 450° and 600 °C, presumably the simultaneous oxidation of molybdenum

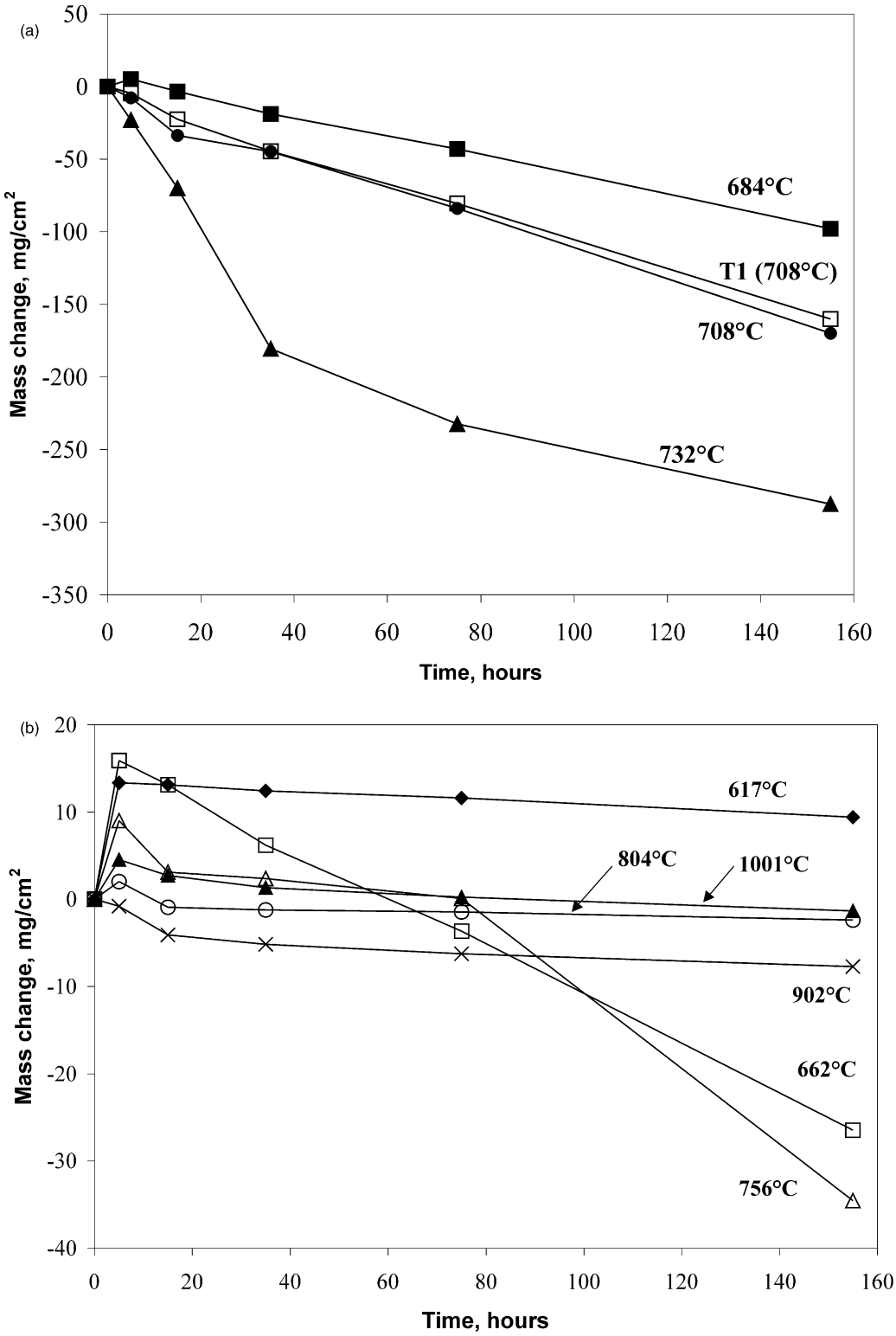

Fig. 8. Oxidation of low-density material for which (a) complete oxidation has occurred by 732 °C, and (b) transitions to both accelerated mass loss and to stable scale formation are observed.

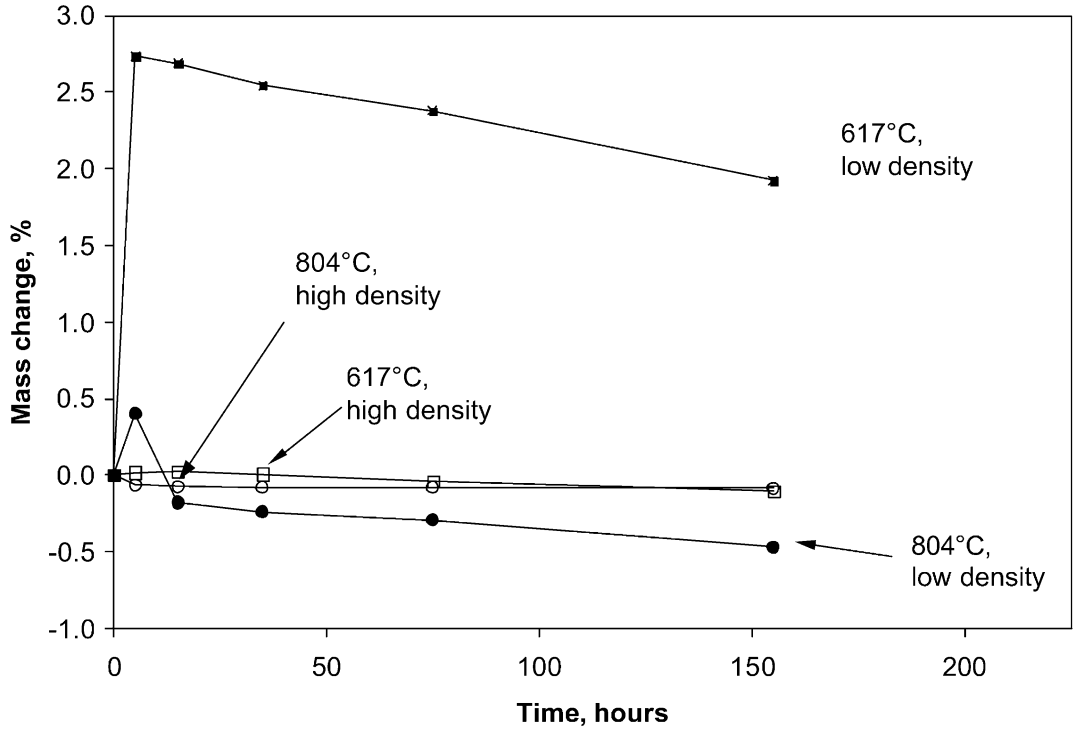

Fig. 9. The effect of sample density on mass loss behavior at the temperatures representing the initial onset and conclusion of accelerated mass loss in low-density material.

and silicon to form MoO_x and SiO_2. The peak structure above 700 °C is less clear. The mass loss indicated in the TG curve corresponds to the evaporation of MoO_3. This is an endothermic event, but the departure from a flat baseline above 700 °C for the low-density sample complicates the assignment of an endothermic peak whose maximum is expected at around 750 °C. Similarly, the small exothermic peak at 730 °C in the high-density material is not understood.

Fig. 8 shows the specific mass change versus exposure time for low-density material. As seen in Fig. 8a, an increasingly large mass loss is observed from 684 to 732 °C. Also tested for comparison was a sample of nearly single-phase T1 that was oxidized at 708 °C. The T1 sample was synthesized by arc-melting and consolidated by traditional powder processing to a theoretical density of greater than 90% [15]. The sample contained a T1 matrix with a small amount of hexagonal Mo_5Si_3. The T1 sample shows similar mass loss behavior as that of the multiphase material, demonstrating that the observed mass loss is dominated by the behavior of the T1 phase. Fig. 8b shows that accelerated mass loss began between 617 and 662 °C and concluded between 756 and 804 °C. High-density material was also oxidized under identical conditions at both 617 and 804 °C, since these temperatures represent the threshold of onset and conclusion of accelerated mass loss. These results are shown in Fig. 9, with mass change plotted as a percentage of the starting mass. The initial mass gain of the low-density sample at 617 °C is significantly larger

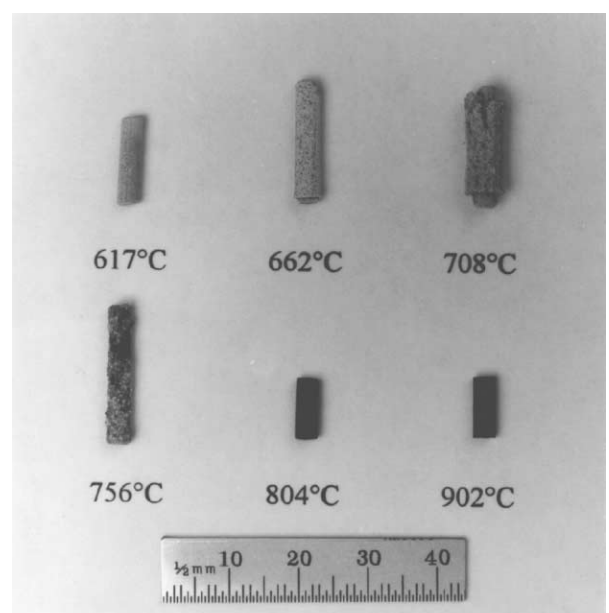

Fig. 10. Macro-view of low-density samples following low temperature oxidation testing. The material completely disintegrated at 732 °C (not shown).

than its counterpart, and this different behavior was previously related to the larger initial surface area of the low-density sample. Qualitative comparison of the rates of oxidation from Fig. 9 shows that at 617 °C, the low-density sample loses mass about five times faster than the high-density sample. At this temperature, neither

material contains a protective borosilicate glassy scale, and so the increased rate is again attributable to the increased surface area of the lower-density sample. At 804 °C the low-density sample at 5 h shows a net mass gain, indicating that the rate of evaporative mass loss of MoO_3 is not sufficient to offset the initial gain due to the oxidation of molybdenum and silicon. The low-density sample at 804 °C loses mass about one-half as fast as that of the low-density sample at 617 °C, and thus a continuous scale has not fully developed at 804 °C. In contrast, the high-density sample at 804 °C shows a near zero rate of mass change. The initial mass gain on heat up is completely lost by the first measurement at five hours, and the near zero rate of mass change indicates that a continuous and protective scale has mostly developed.

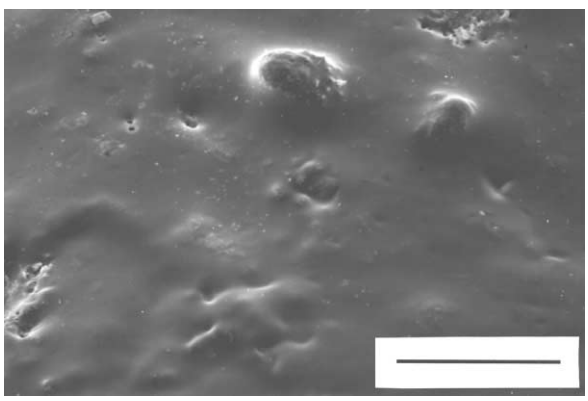

Fig. 11. SEM image (secondary electron) of the surface of the high-density sample oxidized at 804 °C for 155 h. Bar length is 100 μm.

Fig. 10 shows several low-density samples after 155 h of exposure at the indicated temperature. Fig. 10 illustrates the formation of a loosely adherent oxide and sample degradation that progressively worsens from 662 to 708 °C. This process results in complete disintegration of the sample at 732 °C (not shown). XRD analysis of the product formed at 732 °C reveals molybdite MoO_3, JCPDS # 35–609, with residual $MoSi_2$, likely from the starting alloy component. Amorphous silica, though not detectable by XRD, is also expected in the oxide product. Glass formation is visible at 756 °C, and a smooth glassy scale covers the material by 804 °C. SEM examination reveals that a thin, coherent scale less than 10 μm in thickness is formed at 902 °C.

Fig. 11 shows the scale formed on the high-density sample oxidized at 804 °C. EDS analysis of the smooth areas of the scale detects predominantly silicon and oxygen, presumably as silica glass. There are no obvious regions of macro-porosity within the scale, and this indicates that the borosilicate glass has sufficiently formed and reflowed to seal most of the porosity introduced by the volatilization of MoO_3 formed on initial heat up.

3.3. High temperature oxidation behavior

All samples achieve a quasi steady-state oxidation rate following the typical initial mass gain and loss

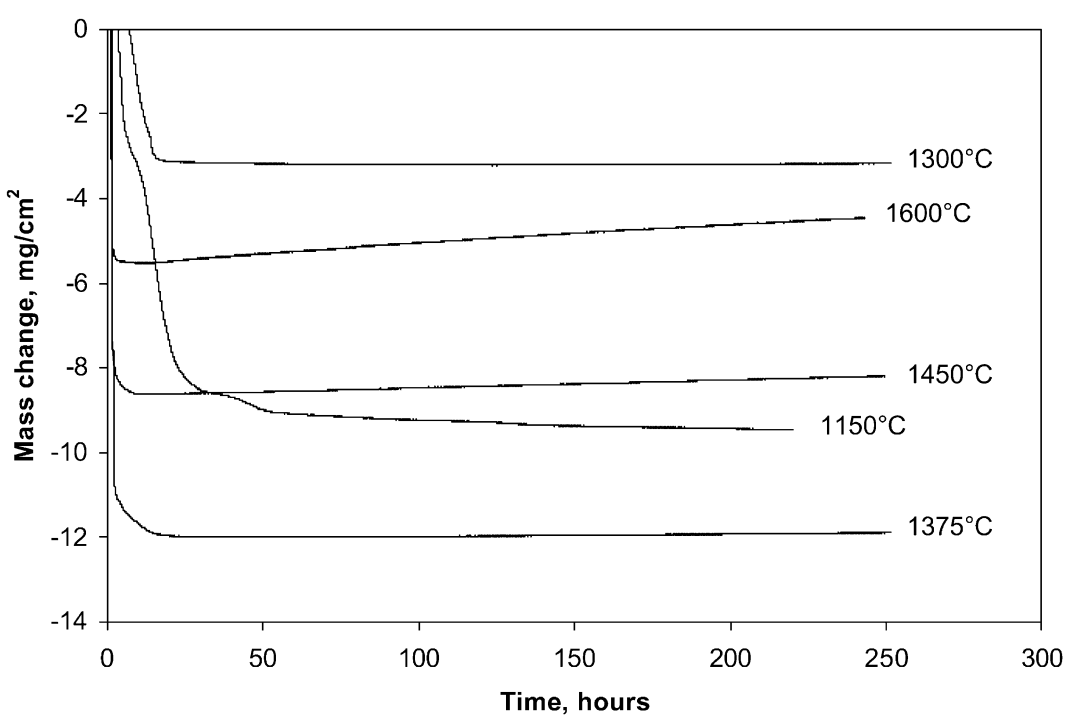

Fig. 12. Mass change of low-density material during oxidation in flowing compressed air at temperatures $T \geqslant 1150$ °C.

shown in Fig. 6. The isothermal mass change of low-density material oxidized from 1150 to 1600 °C is shown in Fig. 12, and to increase clarity, only the portion of the TG curves for a net mass loss are displayed. At 1150 °C a steady-state mass loss is seen, while samples at higher temperatures experience a steady-state mass gain. Fig. 13 shows the cross section of the scale formed on low-density material oxidized at 1300°, 1450°, and 1600 °C. These samples form a coherent, glassy scale with the thickness ranging from 10 to 20 μm. Oxidation within the interconnected porosity is indicated by the presence of glass in much of this porosity. Trapped molybdenum oxide is also visible within these glass-filled pores. Apparently, the tortuosity of the interconnected porosity prevented the complete escape of the volatilized molybdenum oxide before the flowing glass sealed the interior pores from the external surface.

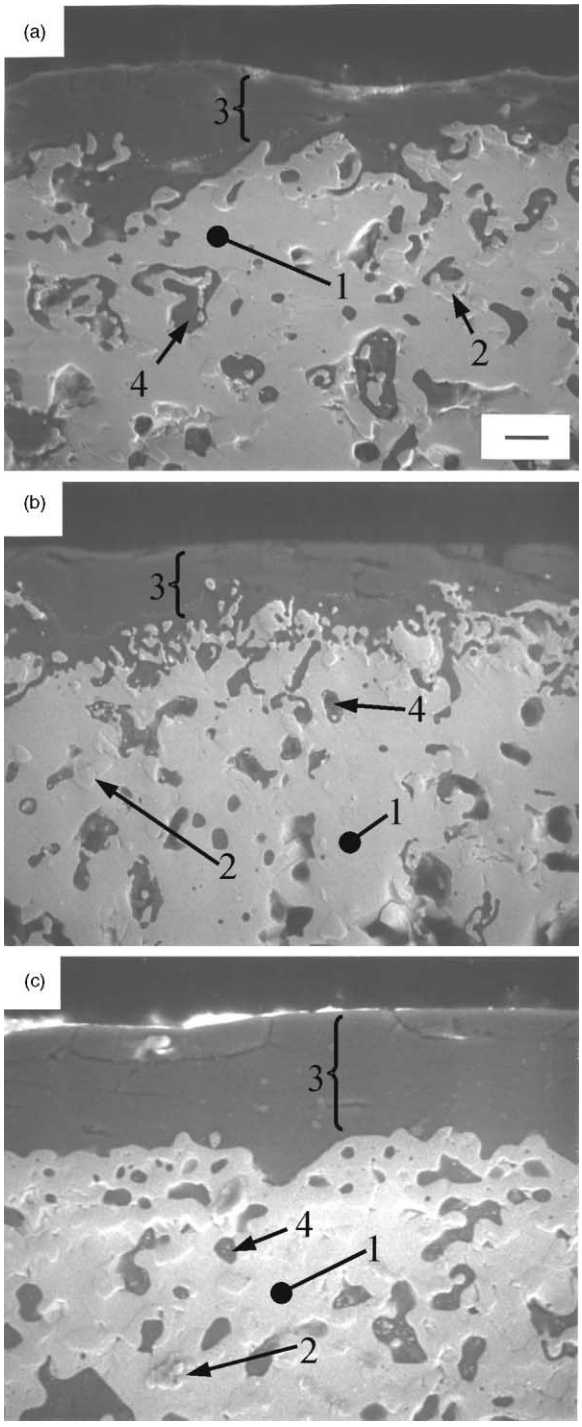

Fig. 13. SEM image (secondary electron) of the cross section of the scale formed on low-density material after oxidation for about 250 h at (a) 1300 °C, (b) 1450 °C, and (c) 1600 °C. Key: 1 = T1 matrix as bright region, 2 = raised MoB grains, 3 = borosilicate scale as darker region, and 4 = glass filled pores containing trapped MoO_3. Bar length is 10 μm.

Steady-state rate constants were calculated by fitting the oxidation data to either a linear or parabolic model. These values are given in Table 1 for each test temperature. Table 1 also gives the time period over which the rate constants for the isothermal mass change were calculated and the mass change observed during that time period. Samples at 1150 and 1600 °C are well described by a linear and parabolic model, respectively. However, samples at 1300, 1375, and 1450 °C show intermediate kinetics, with the mass gain being underestimated by a parabolic model and overestimated by a linear model. Note that up to 1600 °C, the observed steady-state mass change was less than 0.60 mg, where the average sample surface area was about 1 cm^2.

Fig. 14 compares the mass change of both low- and high-density material at 1150 and 1600 °C. Although the low-density material at 1150 °C undergoes a prolonged transient loss, the materials behave kinetically similar at both temperatures. As described in Table 1, at 1150 °C the dense material is well described by linear kinetics, while at 1600 °C the dense material is well described by parabolic kinetics. Shown in Fig. 15, the scale formed at 1150 °C on the low-density sample does not contain visible macro-porosity. EDS of the smooth areas indicates the scale is predominantly silicon and oxygen, presumably as silica. A higher magnification view of the scale, shown previously in Fig. 4, shows that the oxide scale has not completely sealed around the columnar rutile crystals. The underlying alloy likely remains unprotected, and these numerous areas visible

Table 1
High temperature oxidation rate constants

Test temp. (°C)	Sample density	Linear rate constant ($mg/cm^2/h$)	Parabolic rate constant ($mg^2/cm^4/h$)	Steady-state mass change (mg/cm^2)	Time period (h)
1150	Low	L: -1.3×10^{-3}		−0.10	100–250
1150	High	L: -2.9×10^{-4}		−0.04	140–220
1300	Low	L: 3.4×10^{-4}	P: 8.8×10^{-5}	+0.04	140–250
1375	Low	L: 8.0×10^{-4}	P: 4.4×10^{-4}	+0.14	90–250
1450	Low	L: 1.9×10^{-3}	P: 2.4×10^{-3}	+0.25	80–250
1600	Low		P: 1.1×10^{-2}	+0.60	100–250
1600	High		P: 9.7×10^{-3}	+0.55	100–230

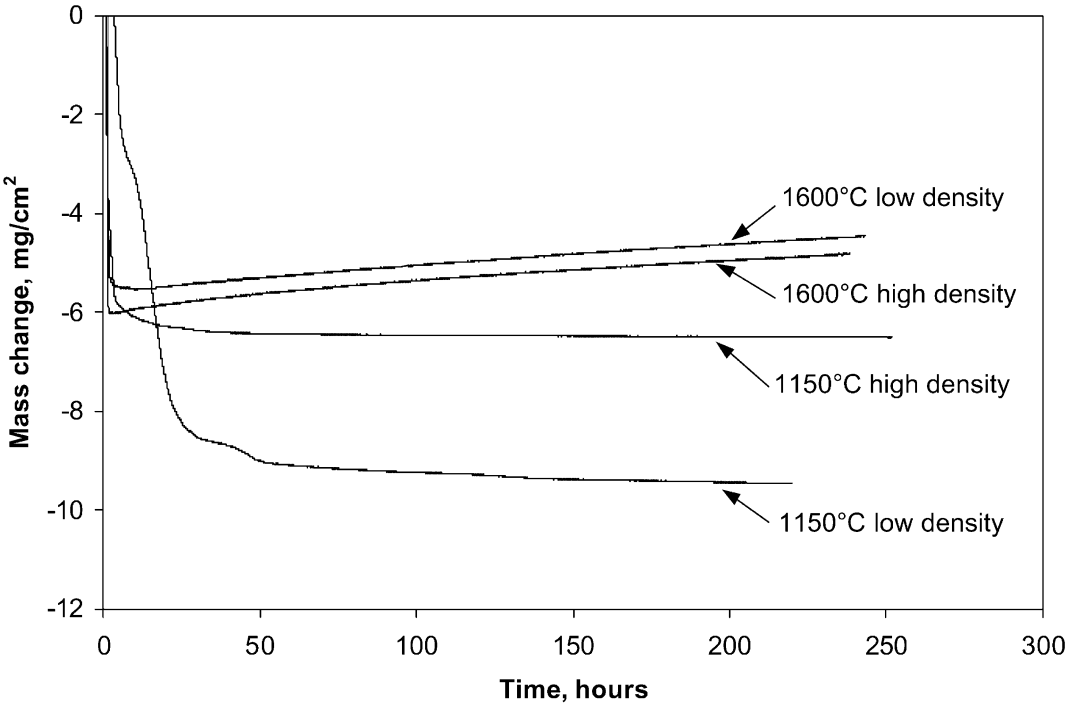

Fig. 14. Comparison of the mass change of low- and high-density material on oxidation at 1150 and 1600 °C.

in Fig. 15 may account for the slow linear mass loss measured at 1150 °C.

For the low-density sample oxidized at 1600 °C, shown previously in Fig. 5, EDS analysis reveals that the smooth areas that are free of the particles are predominantly silicon and oxygen, presumably as silica. Careful analysis of the mass curve in Fig. 12 did not reveal obvious cracking or spalling events during the isothermal test or during cooling to room temperature (not shown in Fig. 12). These particles likely contributed to a tensile loading in the scale during cooling that caused the external portion of the scale to craze. Fig. 13 shows that samples oxidized from 1300 to 1600 °C have cracking at the scale surface that does not penetrate to the scale/alloy interface. This observation is consistent with the quasi steady-state oxidation rates seen in the samples.

In contrast to the low-density sample at 1600 °C, the surface of the high-density sample oxidized at 1600 °C was very smooth and featureless. Fig. 16 shows the edge of the sample where the scale was chipped away to expose the underlying Mo–Si–B alloy. No particles are visible on or in the scale, and EDS analysis shows the scale contains predominantly silicon and oxygen, presumably as silica.

ESCA analysis, shown in Table 2, details the loss of boron from the scale as the exposure temperature increases. The scale formed on the high-density sample oxidized at 804 °C is a boron-rich borosilicate glass. The boron content was 7.8 at.%, and the atomic ratio of oxygen to silicon and boron was 1.83. This compares

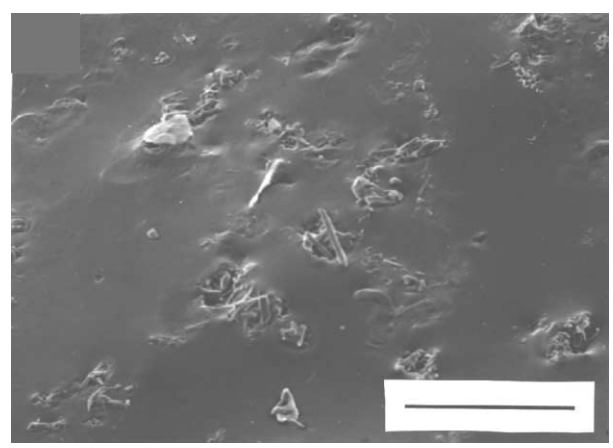

Fig. 15. SEM image (secondary electron) of the surface of the low-density sample, oxidized at 1150 °C for 155 h, showing no visible scale porosity. Bar length is 100 μm.

well to Pyrex® Brand 7740 glass that was measured and found to contain about 5 at.% boron with an oxygen to silicon and boron ratio of 2.03. The expected value [16] is about 7 at.% boron with a ratio of 1.97. From XRD/GSAS analysis of the sintered material, the boron content of the underlying alloy is 8.17 at.%. This indicates that the glass scale is nearly boron saturated with respect to the base alloy. Starting from the boron-rich silica scale formed at 804 °C, boron loss increases dramatically with increasing temperature. The near surface of the scale formed at 1150 °C is significantly depleted of boron, containing only 1.4 at.%. However, the concentration increases rapidly to 3.4 at.% at a depth of

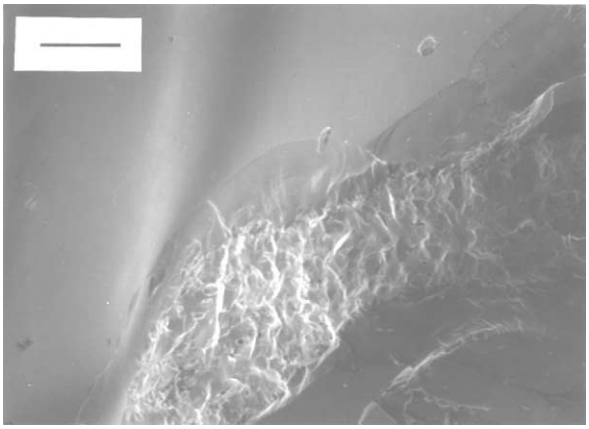

Fig. 16. SEM image (secondary electron) of the surface of the high-density sample oxidized at 1600 °C. The glassy scale was chipped away from the edge of the cylindrical sample, and the fracture surface of the underlying Mo–Si–B alloy is visible. Bar length is 100 μm.

Table 2
ESCA analysis for boron content of silica scale after 200–250 h at temperature

Temperature (°C)	Depth (nm)	O/(Si + B) (atomic ratio)	Boron content (at.%)
804	50	1.83	7.8
1150	18	2.03	1.4
	40	1.99	3.4
1300	40	1.92	0.2
1450	27	1.97	0.0
1600	50	2.04	0.0
1600[a]	50	1.88	0.8

[a] 1 h exposure at 1600 °C.

about 40 nm. The near surface at 1300 °C contains only a trace amount of boron (0.2 at.%), while the near surface is completely depleted at 1450 and 1600 °C. Boron evaporation occurs rapidly, and this was demonstrated in a sample oxidized at 1600 °C for 1 h. The near surface contained only a minor amount of boron (0.8 at.%).

Since the scales were too thick (10–20 μm) for through-scale depth profiling during ESCA measurements, the concentration profile for boron was estimated from an Auger electron line scan profile across the scale cross-section. Fig. 17 shows the combined AES analysis and ESCA analysis of the sample oxidized at 1150 °C. The ESCA analysis of the near surface composition of the scale, already discussed, is shown with an estimated relative uncertainty of ±10%. The AES analysis of the scale cross-section ranges from an approximate depth of 500 to 3200 nm below the surface. Consistency of the data is indicated by the atomic ratio of oxygen to silicon and boron, which ranges from 1.8 to 2.0 for all ESCA and AES measurements. The relative uncertainty of the AES analysis is rather large, approaching 50% (error bars omitted), since a high sensitivity mode was used for the measurement of boron. Accordingly, the concentrations from the AES analysis are useful only on a trend basis. However, taken together, these data show that severe boron depletion that occurs during oxidation at 1150 °C is localized to about the top 50 nm of the scale. Boron content increases appreciably at a depth of about 1500 nm. For reasons already stated, these data are not adequate for analysis of a diffusive mechanism.

4. Discussion

4.1. Low temperature oxidation behavior

The present work agrees well with the previous observations for a similar composition and phase assemblage consolidated by dry pressing and sintering [17]. Meyer et al. found that both silicon and molybdenum oxides had already formed at 600 °C, as detected by XRD and SEM analysis of the surface of the oxidized material, and that formation of MoO_3 increased to a maximum around 725 °C. Significant sublimation occurred by 750 °C, and by 775 °C the surface was a porous borosilicate glass having a lacy network structure. In the present work, a transition to a significant mass loss occurs between 617 and 662 °C, indicating the vapor pressure of MoO_3 has substantially increased. The mass loss progressively worsened until at 732 °C, the sample completely disintegrates. A transition from mass loss to near zero mass change occurs between 756 °C and 804 °C, coincident with the appearance of a glassy surface scale.

Several other authors [18–21] have studied the oxidation behavior of Mo_5Si_3 and shown that the binary silicide undergoes catastrophic oxidation. However, few studies have attempted to determine the susceptibility of boron-modified Mo_5Si_3 (i.e. the T1 phase) to such catastrophic oxidation. The catastrophic degradation observed at 732 °C in the material of this study is morphologically similar to "pest" oxidation observed in $MoSi_2$ at lower temperatures. Many other silicides [22] exhibit this type of behavior, including WSi_2, Nb_5Si_3, and $MnSi_2$. It has been well documented that $MoSi_2$ "pests" in the temperature range of 375–550 °C and is the worst at about 500 °C [23–26]. It is generally believed that pest oxidation is initiated at a structural defect, such as a microcrack or porosity. Formation of SiO_2 and MoO_x oxidation products results in a large volume increase. The large growth stresses create a wedging action that causes crack formation, and the continually increasing surface area accelerates the oxidation process until the material catastrophically degrades. However, "pest" oxidation is not observed in $MoSi_2$ at or above 600 °C at which point a continuous and protective silica layer forms.

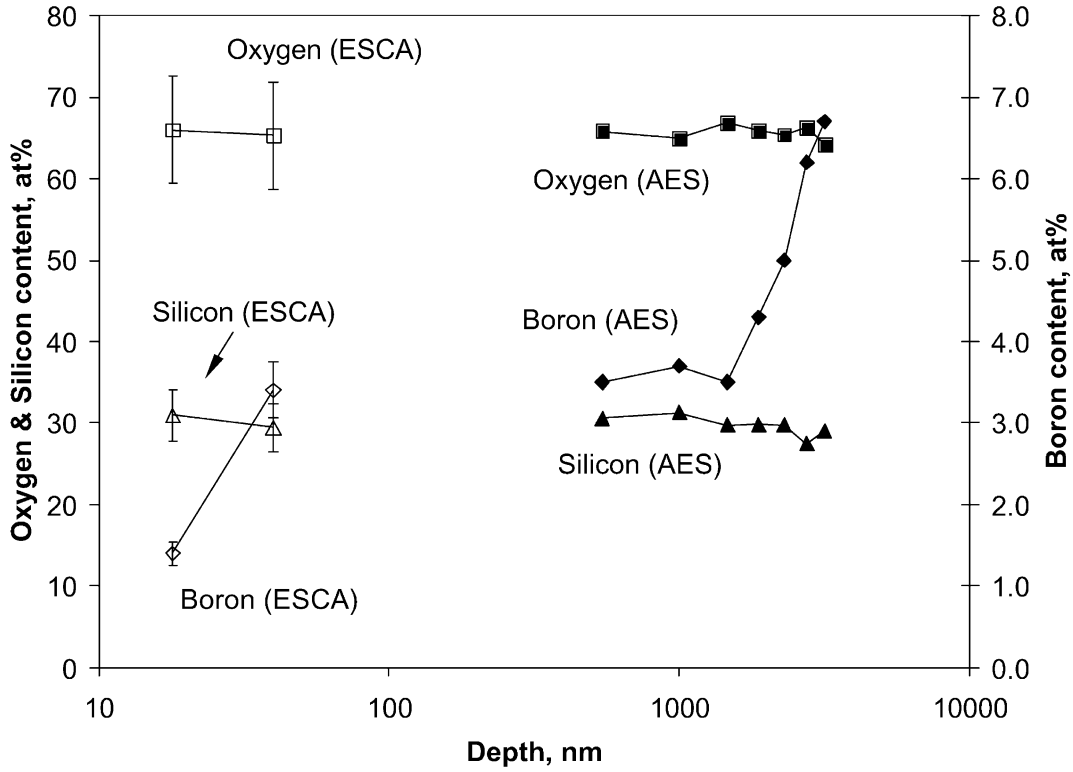

Fig. 17. Trend of silicon, oxygen, and boron content across the scale of high-density material oxidized at 1150 °C. Zero depth is the scale/gas interface.

The catastrophic oxidation observed in the present work is different than the classical "pest" degradation observed in $MoSi_2$. The large mass loss and eventual degradation around 730 °C for the present work is related to the significant consumption of Mo by the rapid formation and subsequent evaporation of MoO_3. The silicon activity in the T1 phase is low and inhibits the formation of a continuous silica layer from 660 to 760 °C. In contrast, $MoSi_2$ forms a continuous silica layer by 600 °C due to the higher activity of silicon in the alloy. The vapor pressure of MoO_3 is much lower near the critical "pest" temperature of about 500 °C for $MoSi_2$. Over the temperature range of 500–750 °C, the vapor pressure of MoO_3 increases by at least four orders of magnitude from about 10^{-2} Pa to 10^2 Pa [27]. Accordingly, the role of MoO_3 in the catastrophic oxidation of $MoSi_2$ is predominantly as a condensed phase. On the other hand, the catastrophic oxidation of $Mo_5Si_3B_x$ is clearly accelerated by the elevated vapor pressure of MoO_3. Near 730 °C, the dominant vapor species over MoO_3 are the trimer, tetramer, and pentamer, whose partial pressures are in the ratio of 11:8:1, respectively [28]. Classic "pest" oxidation as observed in $MoSi_2$ around 500 °C has yet to be observed in the T1 phase. Huebsch [15] examined the low temperature oxidation behavior of T1-based materials at 400 and 600 °C and did not observe catastrophic oxidation. Nonetheless, detailed studies below 600 °C are needed to quantitatively assess the potential of T1-based materials to classically pest.

Aside from the effect of increased surface area on initial mass gain, there is no significant difference in the low temperature oxidation behavior of this material composition due to material density. There is scarce data available to compare to the oxidation rates of the present study. Meyer and Akinc [4] determined the rate constant for a similar composition at 800 °C. The average rate constant over an exposure duration of 280 h was about -3×10^{-4} mg/cm^2/h. The initial surface area of the high-density sample at 804 °C can be reasonably calculated, and the rate constant based on four mass measurements for $t\geqslant35$ h from Fig. 9 is -2×10^{-3} mg/cm^2/h. The limited number of data points precludes a statistically valid comparison. However, the continued slow, but measurable mass loss suggests the continued evaporation of MoO_3 in both samples. SEM/EDS analysis did not reveal porosity or suggest MoO_3 formation in the scale of either sample. ESCA measurements of the high density sample at 804 °C did detect about 0.4 at.% molybdenum in the scale. High resolution SEM investigation of the scale is needed to better detect possible nano-porosity that could be responsible for MoO_3 evaporation. Meyer et al. [17] reasoned that at 800 °C, a porous borosilicate glassy scale with fine pores on the order of 0.1 μm would exhibit Knudsen-type diffusion of oxygen and MoO_3. The time scale for viscous flow to

completely seal the surface would be dependent on the viscosity of the scale, which is a strong function of its boron content. For the present study, the material at 804 °C has a boron to silicon ratio of 0.28, and this is similar to Pyrex® Brand 7740 glass. The viscosity for Brand 7740 glass is given by Eq. (1), where η is viscosity in Poise and T is temperature in K [29].

$$\log\eta = 1.7 \times 10^4 T^{-1} - 7.5 \times 10^1 \quad (1)$$

The estimated scale viscosity at 800 °C is 2.6×10^7 Pa·s, and this is near the softening point for the glass. Thus for an extended hold time, flow of the scale to seal the surface is expected. MoO_3 will quickly move through the scale when a bubble reaches a critical size that balances the capillary force due to surface tension against the vapor pressure of MoO_3. While there is no direct evidence of this at 804 °C for this composition, it has been observed in Mo-rich alloys. Parthasarathy et al. [30] observed MoO_3 to bubble through the scale of the alloy Mo–12B–12Si (at.%) oxidized at 800 °C. The high boron content of the alloy leads to the formation of a boron-rich scale, estimated to be 33 mol% B_2O_3 in SiO_2. The lower viscosity of this scale enabled the movement of bubbles through the scale.

4.2. High temperature oxidation behavior

Loss of boron from borosilicate glass at elevated temperatures is well documented, while at lower temperatures, the volatility is not significant. Taylor et al. [31] investigated sol-gel derived borosilicate glasses containing about 5.5 at.% boron and found no boron loss during heat treatments at 840 °C. The atmosphere, though not specified, is assumed to be ambient air. This is consistent with our findings for material oxidized at 804 °C. Buchanan et al. [32] found that borosilicate glass containing 9.5 at.% boron lost about 5 wt% (absolute basis) after 20 h at 1100 °C in wet air. The mechanism of boron loss was assumed to be the formation of volatile HBO_2. Vance et al. [33] examined French AVM-type borosilicate glasses containing about 14 at.% boron. On exposure at 1250 °C for 24 hours in air, the fractional loss of boron was 12%, and the presumed volatilized species was an alkali-based borate. The borosilicate scale of the present work is void of a measurable quantity of alkali glass modifiers, neglecting the Ca contamination, and the oxidation experiments were performed in flowing breathing-quality air that contains trace amounts of water. The mode of boron loss is most likely the evaporation of a non-hydrated borate.

The change in scale chemistry seen during increasing exposure temperatures complicates understanding the mechanism of oxidation for Mo–Si–B composites. At lower temperatures, the higher boron content of the scale aids in the initial formation of a continuous glassy scale. Meyer did find boron depletion of the scale after long exposures at 1000 °C. From the present work, the high boron content at 804 °C significantly decreased as temperature increased, and at 1150 °C, a concentration gradient of boron was measured through the scale. The extent of boron depletion was localized to the near surface, and though not measured, the depletion zone likely extends to a much greater depth into the scale at higher temperatures. The outer portion of the scale becomes pure silica, and oxygen transport through pure silica is known to be much slower than through boron-modified silica. Slower diffusion through the outer silica layer should become the rate-limiting step in the oxidation process. Depending on the oxidation temperature and the extent of boron enrichment of the scale near the scale/alloy interface, the lower relative viscosity of the glass in this area may enable the formation of bubbles at the interface. As previously discussed, MoO_3 bubble formation was observed in a Mo-rich alloy, Mo–12B–12Si, whose scale was estimated to contain 33 mol% B_2O_3 [30]. For the present alloys, Meyer has shown that transport of oxygen through these scales is sufficiently slow that elemental molybdenum can form at the interface. MoO_3 does not form, and thus bubble formation is minimized. The high viscosity silica near the scale/gas interface forms a high viscosity shell that resists the flow of the lower viscosity scale nearer to the scale/alloy interface.

Fig. 18 shows an Arrenhius plot of the calculated parabolic rate constants with the rates from the previous work by Meyer et al. also plotted [4,5]. Over the temperature range of 1050–1300 °C, the activation energy reported by Meyer was 134 kJ/mole, and the additional data of Meyer at 1450 °C agrees reasonably well with the extrapolated trend. Schlichting [34] determined an activation energy of 138 kJ/mol for oxygen diffusion through sol-gel derived borosilicate glass, and based on these data, Meyer explained the rate-limiting step to likely be oxygen diffusion through a coherent borosilicate glass scale. For the present work, only the rate at 1375 °C compares well with the trend from Meyer. It should be noted, however, that the plot for the present work is useful only for comparative purposes since the rate kinetics for the present work are influenced by the presence of processing-related contaminants. In particular, the rate kinetics for the oxidation of titanium are much faster and would contribute to a rapid linear mass gain. Given the non-negligible levels of titanium observed in the scales, the higher rates observed at 1450 and 1600 °C likely reflect this contribution.

More detailed diffusion studies are needed to better understand the oxidation process in this system. Unfortunately, measuring activation energies through kinetic studies cannot definitively determine the probable

rate-limiting step for oxidation in these materials. Meyer's measured activation energy of 134 kJ/mol, which agreed well with the value of 138 kJ/mol obtained by Schlichting, is also in the range for oxygen diffusion through vitreous silica [35]. Careful measurement of boron, silicon, and oxygen chemistry through the scale as a function of oxidation temperature is needed to better understand and model mass transport through these scales.

Fig. 19 compares the oxidation at 1600 °C of high-density material to that of a Kanthal Super 33® heating element ($MoSi_2$-based material). To simplify the

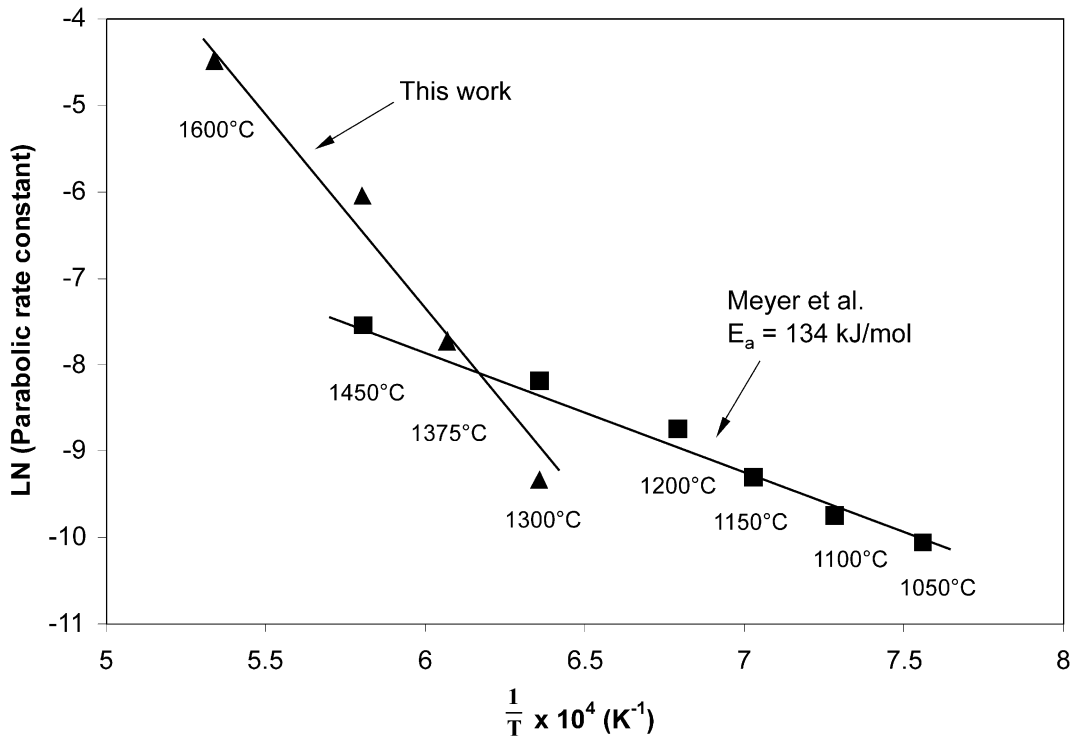

Fig. 18. Arrenhius plot comparing the parabolic rate constants calculated from the present work to that of Meyer et al. [4,5].

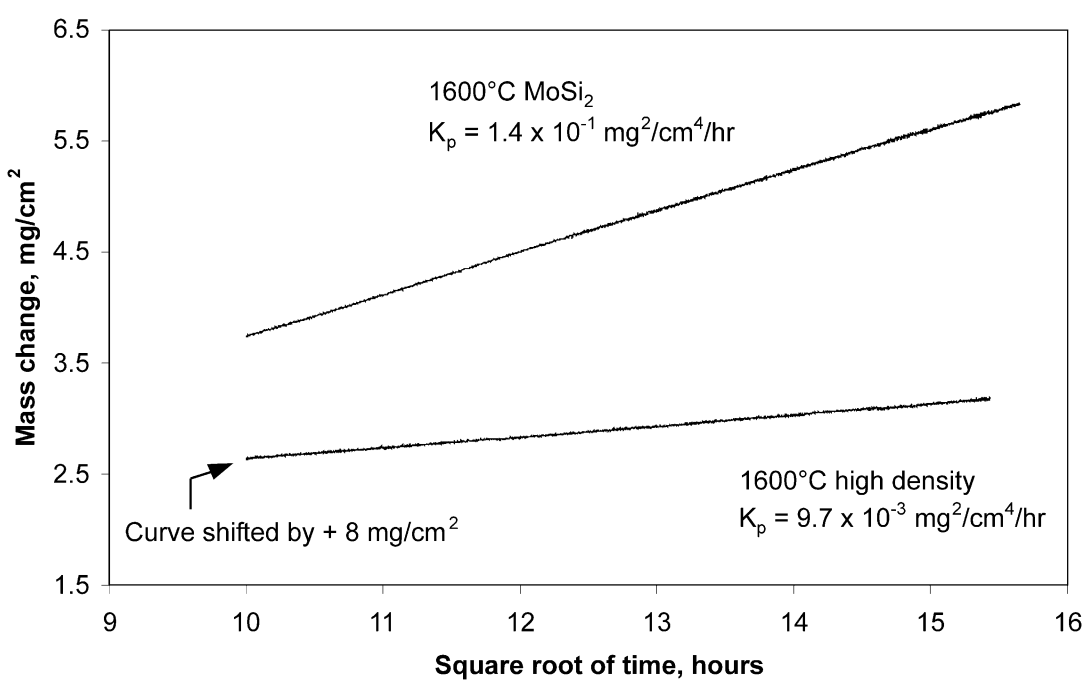

Fig. 19. Comparison of the oxidation at 1600 °C of high-density material and Kanthal Super 33® heating element material.

comparison, the mass curve of the high-density sample was shifted by +8 mg/cm^2. The calculated parabolic rate constant for the high-density material is actually lower than that of the Kanthal material, demonstrating that T1-based materials show adequate oxidative stability as required for long term use as a heating element material.

5. Summary

This work confirmed the excellent oxidation resistance of Mo–Si–B composites based on the $Mo_5Si_3B_x$ phase that are fabricated by a green extrusion process. These materials demonstrated excellent oxidation resistance to at least 1600 °C, with rate kinetics comparable to and even better than $MoSi_2$-based heating element materials. Consistent with previous results for sintered materials, this work has shown that T1-based compositions form a protective glassy scale at temperatures above about 760 °C. These materials are susceptible to accelerated oxidation from about 660 to 760 °C, and complete disintegration occurs near about 730 °C. This process differs from classic "pest" oxidation since it is related to the elevated vapor pressure of MoO_3 and the continuous loss of molybdenum from the alloy. The scale formed at 800 °C is a boron-rich borosilicate glass, and thus oxygen diffusion through borosilicate glass must be the rate-limiting step near 800 °C. Boron depletion of the scale is observed at 1150 °C with the near surface becoming completely depleted by 1450 °C. This boron loss has no detrimental effect upon the ability of the alloys to form protective scales at high temperatures. Boron evaporation from the outer scale results in the formation of pure silica, and this implies that oxygen transport through silica must be the rate-limiting step for high temperature oxidation. More thorough studies are required to better understand the mechanism of oxidation in these alloys.

Acknowledgements

This manuscript has been authored by Iowa State University of Science and Technology under contract No. W-7405-ENG-82 with the U.S. Department of Energy. The United States Government retains and the publisher, by accepting the article for publication, acknowledges that the United States Government retains a non-exclusive, paid-up, irrevocable, worldwide license to publish or reproduce the published form of this manuscript, or allow others to do so, for United States Government purposes. Ames Laboratory is operated for the U.S. Department of Energy by Iowa State University under contract number W-7405-ENG-82. This research was supported by the Office of Basic Energy Science, Materials Science Division. This research was also supported by the Office of Energy Research, Office of Computational and Technology Research, and the Advanced Energy Projects Division. The authors thank Jim Anderegg for the ESCA measurements and Vince Crist for the AES measurements.

References

[1] Massalski TB et al., editors. In: Binary alloy phase diagrams, vol. 3. Materials Park (OH): American Society of Metals; 1990. p. 2666.
[2] Whychell D. Bloomfield (NJ): CM Furnaces; 1999.
[3] Meyer MK, Kramer MJ, Akinc M. Compressive creep behavior of Mo_5Si_3 with the addition of boron. Intermetallics 1996;4:273–81.
[4] Meyer MK, Akinc M. Oxidation behavior of boron-modified Mo_5Si_3 at 800–1300 °C. J Am Ceram Soc 1996;79(4):938–44.
[5] Meyer MK, Akinc M. Isothermal oxidation behavior of Mo-Si-B intermetallics at 1450 °C. J Am Ceram Soc 1996;79(10):2763–6.
[6] Akinc M. Next generation high-temperature structural materials for heat exchangers and heating elements. Final report. Advanced Energy Project Agency, Energy Research, U.S.D.O.E.; 1999.
[7] Sakidja R, Sieber H, Perepezko JH. Microstructural development of Mo-rich Mo-B-Si alloys. TMS Molybdenum and Molybdenum Alloys Symposium Proceedings, 1998. p. 99–110.
[8] Nunes CA, Sakidja R, Perepezko JH. Phase stability in high temperature Mo-rich Mo-B-Si alloys. In: Nathal MV et al., editors. Structural intermetallics. 1997. p. 831–839.
[9] Schneibel JH, Liu CT, Easton DS, Carmichael CA. Microstructure and mechanical properties of Mo-Mo_3Si-Mo_5SiB_2 silicides. Materials Science and Engineering 1999;A261:78–83.
[10] Schneibel JH, Kramer MJ, Unal O, Wright RN. Processing and mechanical properties of a molybdenum silicide with the composition Mo-12Si-8.5B (at.%). Intermetallics 2001;9(1):25–31.
[11] Schneibel JH, Liu CT, Heatherly L, Kramer MJ. Assessment of processing routes and strength of a 3-phase molybdenum boron silicide (Mo_5Si_3-Mo_5SiB_2-Mo_3Si). Scripta Materialia 1998;38(7):1169–76.
[12] Joint Molybdenum Silicide Alloy Research Meeting between representatives from Air Force, Navy, Pratt & Whitney, USDOE, and associated Universities. TMS Conference, Cincinnati, OH, 4 November 1999.
[13] Summers E, Thom AJ, Cook BA, Akinc M. Extrusion and selected engineering properties of Mo-Si-B intermetallics. Intermetallics 2000;8/9(11):1169–74.
[14] Summers E. Processing of Mo-Si-B intermetallics by extrusion and oxidation properties of the extruded T1-$MoSi_2$-MoB system. Masters thesis, Iowa State University, Ames, IA, 1999.
[15] Huebsch JJ. Solubility of boron in $Mo_{5+y}Si_{3-y}$ and related mechanical and oxidation properties. Masters thesis, Iowa State University, 1998.
[16] Corning Life Sciences Technical Information Center webpage for Pyrex® Brand 7740 glass. Available from: http://www.scienceproducts.corning.com/technical/descglasslabware.asp#7740LowExpansion.
[17] Meyer MK, Thom AJ, Akinc M. Oxide scale formation and isothermal oxidation behavior of Mo-Si-B intermetallics at 600–1000 °C. Intermetallics 1999;7:153–62.
[18] Berkowitz-Mattuck J, Dils R. High temperature oxidation II. Molybdenum silicides. J Electrochem Soc 1965;112(6):583–9.
[19] Bartlett R, McCamont J, Gage P. Structure and chemistry of oxide films thermally grown on molybdenum silicides. J American Cer Soc 1965;48(11):551–8.
[20] Anton D, Shaw D. High temperature properties of refractory intermetallics. Mat Res Soc Symp Proc 1991;213:63–8, 733–39.

[21] Thom AJ, Meyer MK, Williams JJ, Akinc M. Improved oxidation resistance of A_5Si_3 (A = transition metal) silicides by small atom doping. Processing and Fabrication of Advanced Materials IV 1996. p. 139–49.
[22] Yanagihara K, Maruyama T, Nagata K. Effect of third elements on the pesting suppression of Mo-Si-X intermetallics (X = Al, Ta, Ti, Zr, and Y). Intermetallics 1996;4:S133–139.
[23] Smialek JL, Nesbitt JA, Brindley WJ, Brady MP, Doychak J, Dickerson RM, Hull DR. Service limitations for oxidation resistant intermetallic compounds. Mat Res Soc Symp Proc 1995;364: 1273–84.
[24] Lee EW, Cook J, Khan A, Mahapatra R, Waldman J. The oxidation resistance of $MoSi_2$ composites. J Metals 1991;43(3):54–7.
[25] Chou TC, Nieh TG. Kinetics of $MoSi_2$ pest during low-temperature oxidation. J Mat Res 1993;8(7):1605–10.
[26] Chou TC, Nieh TG. Mechanism of $MoSi_2$ pest during low-temperature oxidation. J Mat Res 1993;8(1):214–25.
[27] Samant MS, Kerkar AS, Bharadwaj SR, Dharwadkar SR. Thermodynamic investigation of the vaporization of molybdenum trioxide. J Alloys Compounds 1992;187:373–9.
[28] Brewer L, Lamoreaux RH. In: Brewer L, editor. Molybdenum: physico-chemical properties of its compounds and alloys, in Atomic Energy Review, Special Issue 2, 1980.
[29] Properties of Corning's glass and glass ceramic families. Corning Glass Works, December 1979.
[30] Parthasarathy TA, Mendiratta MG, Dimikuk DM. Oxidation mechanisms of Mo-reinforced Mo_5SiB_2 (T2)–Mo_3Si alloys. Acta Materialia 2002;50(7):1857–1868.
[31] Taylor DJ, Dent DZ, Braski DN, Fabes BD. Boron loss in furnace- and laser-fired, sol-gel derived borosilicate glass films. J Mat Res 1996;11(8):1870–3.
[32] Buchanan FJ, Little JA. Glass sealants for carbon-carbon composites. J Mat Sci 1993;28:2324–30.
[33] Vance ER, Hayward PJ, Hamon RF. Volatile losses from sphene glass-ceramic and borosilicate glass melts. J Amer Cer Soc 1988; 71(7):C318–0C320.
[34] Schlichting J. Oxygen transport through glass layers formed by a gel process. J Non-Crystall Solid 1984;63:173–81.
[35] Kalen JD, Boyce RS, Cawley JD. Oxygen tracer diffusion in vitreous silica. J Am Ceram Soc 1991;74(1):203.